Helical Level Structure of Dirac Potential Wells

Daniel Walkup[1,2†] and Joseph A. Stroscio[1]

[1]Center for Nanoscale Science and Technology, National Institute of Standards and Technology, Gaithersburg, MD 20899, USA
[2]Maryland NanoCenter, University of Maryland, College Park, MD 20742, USA

Abstract

In graphene and other massless two-dimensional Dirac materials, Klein tunneling compromises electron confinement, and momentum-space contours can be assigned a Berry phase which is either zero or π. Consequently, in such systems the energy spectrum of circular potential wells exhibits an interesting discontinuity as a function of magnetic field B: for a given angular momentum the ladder of eigen-resonances is split at an energy-dependent critical field B_c. Here we show that introducing a mass term Δ in the Hamiltonian bridges this discontinuity in such a way that states below B_c are adiabatically connected to states above B_c whose principal quantum number differs by unity depending on the sign of Δ. In the B-Δ plane, the spectrum of these circular resonators resembles a spiral staircase, in which a particle prepared in the $|n, m\rangle$ resonance state can be promoted to the $|n \pm 1, m\rangle$ state by an adiabatic circuit of the Hamiltonian about B_c, the sign depending on the direction of the circuit. We explain the phenomenon in terms of the evolving Berry phase of the orbit, which in such a circuit changes adiabatically by 2π.

† daniel.walkup@nist.gov

Introduction. The lightlike carriers in graphene allow optics-inspired analogies such as reflection, refraction, and resonators, to be realized using confining electrostatic potentials and magnetic fields. Tailoring electrostatic *p-n* junctions have demonstrated geometries with linear boundaries mimicking Fabry-Perot etalons [1] and circular *p-n* junctions have demonstrated the classical analogy of whispering gallery modes [2–4]. A key difference between the wave properties of graphene carriers, and the carriers of conventional two-dimensional electron gases, is the associated chirality and nontrivial Berry phase of the graphene wavefunctions. Chirality and Berry phase in the massless Dirac Hamiltonian describing graphene was recognized in the first experimental papers describing the graphene quantum Hall effect [5,6], and date back to the work in carbon nanotubes [7]. In the Fabry-Pèrot geometry it was shown that the transport conductance underwent a phase shift with the application of a magnetic field, which is traceable to the graphene π Berry phase [8]. More recently, it has been shown that in circular *p-n* junction geometries, resembling quantum dots (QDs), the graphene eigenstates show a discontinuity at a weak critical magnetic field, B_c, which was predicted by theory and confirmed in recent measurements [4,9]. This spectral discontinuity, and its resolution with the addition of a mass term, Δ, is the focus of this work. We show in detail that in the three-dimensional space of B, Δ and energy, the spectrum resembles a continuous helical sheet, the successive energy levels of which can be accessed by adiabatic circuits about the discontinuity in the B-Δ plane.

The electronic structure of graphene or two-dimensional (2D) Dirac quantum dots has been extensively studied in a wide range of models [10–18]. The arguments given here are applicable to any radially symmetric, monotonic, smoothly varying potential. For concreteness, in the calculations we use a quadratic confining potential, which has been shown to adequately capture the experimental spectrum of graphene QDs measured by scanning tunneling spectroscopy [2,19],

including the Berry phase discontinuity [4]. The helical connectivity of the eigenstate structure is first shown using classical arguments, combined with a consideration of Berry phase. Then, we exhibit the helical spectrum using quantum-mechanical calculations along cuts through the B-Δ plane. Finally, we calculate the eigenresonances along an elliptical loop surrounding B_c, showing how a picked quantum state would evolve from $|n, m\rangle$ to $|n-1, m\rangle$ along an adiabatic circuit.

Semiclassical analysis. The classical 2D relativistic Hamiltonian for a central potential $U(r)$ can be expressed in polar coordinates as

$$H(r, p_r, \phi, p_\phi) = \pm v_F \sqrt{{p_r}^2 + \left(\frac{p_\phi}{r} - \frac{eB}{2} r\right)^2 + \left(\frac{\Delta}{v_F}\right)^2} + U(r), \tag{1}$$

where v_F is the Fermi velocity, Δ/v_F^2 is the mass, U is the potential energy, and e is the elementary charge. The angular momentum p_ϕ is conserved. For calculations, we take v_F = 10^6 m/s, and $U = \kappa r^2$where $\kappa = 4$ eV/μm^2. The trajectories of Eq. (1) twist at a critical field B_c [9], as shown in Figs. 1(a)-1(c). The transition between the left-turning particle [Fig. 1(a)] and the right-turning, looping particle [Fig. 1(c)] involves an intermediate state in which the particle must stop completely and turn back [Fig. 1(b)]. If $\Delta = 0$, we encounter the result that backscattering is forbidden for massless Dirac particles: they do not orbit, but escape the well by Klein tunneling [17,20–22] [Fig. 1(d)]. With finite Δ, however, the classical orbit continues [Fig. 1(e)], and the corresponding quantum states acquire a nonzero lifetime, which can be estimated from the transmission coefficient for Klein-tunneling through a sloped potential barrier. This being $e^{-C\Delta^2}$ [22,23] (where C is a constant that depends on the barrier slope), we see that while at $(B_c, \Delta = 0)$ the eigenstate spectrum must be discontinuous, for finite Δ the discontinuity is bridged

by quasi-bound states [9], whose stability increases super-exponentially with $|\Delta|$. (Hereafter, the $\Delta = 0$ singular point is denoted simply by B_c.)

The helical eigenstate structure reported here arises from the fact that these finite-Δ "bridges" connect *different* eigenstates depending on the sign of Δ. This is shown directly in Fig. 3, but can be motived classically by combining the adiabatic theorem [24] with a semiclassical consideration of the Berry phase [9]. Let us start the classical particle in some Hamiltonian [Eq. (1)] defined by (B_0, Δ_0), with arbitrary initial coordinates and momenta, and adiabatically vary B and Δ. In the volume defined by B, Δ, and the energy E, the particle is constrained to move on a sheet defined by the condition $J_r(E) \equiv \oint p_r(r)dr$ = constant. The Berry phase φ_B is included via the modified Bohr-Sommerfeld quantization condition:

$$J_r(E) = 2\pi\hbar\left(n - \frac{\varphi_B}{2\pi} + \gamma\right), \tag{2}$$

where n is the radial quantum number and γ is a constant, here equal to ½ [25,26]. A consistent semiclassical method for calculating φ_B in this system is given in Ref. [9], and summarized below: The quantum Hamiltonian $H = v_F \mathbf{\Pi} \cdot \boldsymbol{\sigma} + \Delta\sigma_z + U(r)$ (where $\mathbf{\Pi}$ is the kinematic momentum and $\boldsymbol{\sigma}$ the Pauli matrices) has a monopole Berry curvature field $\mathbf{\Omega}(\mathbf{h}) = \frac{1}{2}\mathbf{h}/h^3$, where $\mathbf{h} = (\Pi_x, \Pi_y, \Delta/v_F)$. To each classical orbit belongs a closed $\mathbf{h}$-space loop Γ, and φ_B is the flux of $\mathbf{\Omega}$ through Γ, in this case one-half the solid angle it subtends [27]. To calculate Γ, one resorts to Einstein-Brillouin-Keller (EBK) quantization [9,28,29]. This procedure defines the action variables J_i as line integrals along the closed surface contours of a phase-space torus. By evaluating $\mathbf{h}$ along the same contours, a closed Γ can be consistently obtained [9]. Further, J_r retains the definition given above, and the resulting φ_B can be directly applied to Eq. (2). Thus it was found that, taking B_c positive and $\Delta = 0$, for $B < B_c$ Γ lies entirely to one side of the origin, subtending

zero solid angle and providing zero Berry phase [Fig. 2(a)], whereas for $B > B_c$ it encircles the origin, providing a Berry phase of π as in the case of pure Landau levels (LLs) [9]. At $\Delta = 0$, the result is a discontinuous jump of the energy levels by half a level, which was observed experimentally [4].

From the above we see that by adiabatically varying B and Δ, we can manipulate Γ to produce an unlimited tunability of φ_B in Eq. (2). Starting for concreteness at an initial Hamiltonian defined by $(B < B_c, \Delta = 0)$, let us see what happens as we attempt a clockwise adiabatic circuit about B_c (Fig. 2) As we pass over [Fig. 2(b)], down around [Fig. 2(c)], and back underneath the critical point [Fig. 2(d)], we see that Γ (thin blue line) loops over and around the monopole source of Berry curvature in such a way that the solid angle (light blue membrane) increases smoothly from zero in Fig. 2(a) to 4π in Fig. 2(d), so that φ_B grows by 2π. At the classical level, this procedure is fully reversible and repeatable: A second pass over the circuit would make the bubble two layers thick (8π solid angle), a reverse circuit would unwrap one layer of the bubble, and so on. The effect of one circuit is to change the right side of Eq. (2) by $2\pi\hbar$ and, the other terms being constants, the same change must appear in J_r: an adiabatic circuit changes the "effective" radial quantum number by one. Thus when Berry phase is included, the constant-action sheet of the classical particle becomes a connected, multilevel helical manifold in the B-Δ plane, each level of which can be accessed from any other level by repeated circuits about the screw dislocation at B_c.

Quantum simulation and results. To explore this helix structure quantitatively, we performed calculations based on the "spectral method" [30], adapted for 2D Dirac particles. In this procedure, an essentially arbitrary initial wave function $\Psi(\mathbf{r}, 0)$ is evolved numerically under the time-dependent Schrödinger equation. In general, $\Psi(\mathbf{r}, 0)$ will have matrix elements with all

possible solutions of the Schrödinger equation: bound or quasibound states, and continuum states. During evolution, the latter quickly propagate to the edge of the simulation area, where they are absorbed, while the former oscillate with their characteristic frequencies $\omega_n = -E_n/\hbar$. These frequencies are extracted post-evolution from the power spectrum of $C(t) \equiv \langle \Psi(0)|\Psi(t)\rangle$, and the eigenstates $\psi(\mathbf{r}; E_n)$ are obtained by Fourier-filtering $\Psi(\mathbf{r}, t)$ at the corresponding frequency [30]. This enables us to characterize the spectrum of the 2D Dirac Hamiltonian without any *a priori* assumptions, except those which govern the form of the initial wavepacket (see below). Moreover, the inherently dynamic nature of the method allows us to directly enact the adiabatic loops discussed above by evolving a particle, prepared in some eigenstate, in a slowly-varying Hamiltonian .

The time evolution is performed via the third-order [31] split-operator method [32,33], using the 2D Dirac Hamiltonian

$$H(\mathbf{k}, \mathbf{r}) = \hbar v_F \begin{pmatrix} 0 & k_x - ik_y \\ k_x + ik_y & 0 \end{pmatrix} + \begin{pmatrix} U + \Delta & -v_F e\left(A_x - iA_y\right) \\ -v_F e\left(A_x + iA_y\right) & U - \Delta \end{pmatrix} \quad (3)$$

where A_x, A_y, and U are functions of $\mathbf{r}$, $\mathbf{k} = \mathbf{p}/\hbar$, and the vector potential is taken in the symmetric gauge. Because the helical spectrum is a property of H at a fixed angular momentum, to obtain it we should choose an initial wavefunction of the form

$$\Psi_m(\mathbf{r}, 0) = e^{i\left(m - \frac{1}{2}\right)\phi} \begin{pmatrix} u_0(r) \\ e^{i\phi} u_1(r) \end{pmatrix}, \quad (4)$$

where $m\hbar$ is the angular momentum, m is an odd-half integer, and u_0 and u_1 are arbitrary functions containing a broad spectrum of wavelengths. The energies of the spectral peaks are completely insensitive to the choice of u_0 and u_1 within very broad limits; their amplitudes, however, can vary

considerably due to matrix element effects. A "good" choice of the u_i provides distinctly nonzero matrix elements with all $|n, m\rangle$ states up to some n_{max}, determined by the shortest wavelength in the u_i, for all (B, Δ) which we wish to study; the spectra of Fig. 3 were obtained with such a function [34].

In Fig. 3 we show resonance spectra of the same initial wave function, for m=5/2, as a function of magnetic field obtained at three characteristic masses less than [Fig. 3(a)], equal to [Fig. 3(b)], and greater than [Fig. 3(c)] zero. As a guide to the eye we include those regions of the (B, E) plane in which classical periodic motion is possible (dark red) or impossible (dark blue), determined by analyzing the function $p_r^2(r)$ extracted from the Hamiltonian in Eq. (1) [34]. For high positive fields [right edge of Figs. 3(a)-3(c)] the spectra resemble the well-known quantum Hall energy spectrum: an N=0 LL at energy Δ, which at $\Delta = 0$ bridges the positive and negative LLs whose energies are proportional to $\sqrt{|N|}$. Visually, the movement of this state as a function of Δ is the key to the helix structure. For $\Delta < 0$ the N=0 LL attaches to the group of negative LLs, so that the lowest "positive energy" LL is N=1 [Fig. 3(a)], whereas for $\Delta > 0$ the N=0 state is the lowest positive LL [Fig. 3(c)] [35]. Following our classical discussion, we see that for nonzero mass all the positive-energy states are adiabatically continuous as a function of B: we can re-enact the circuit of Fig. 2 by picking some initial state and sliding along the resonance curves. A brief inspection shows that such a circuit, beginning in state **A** of Fig. 3(b), passes to state **B'** in Fig. 3(c), thence to state **B** in Fig. 3(a) and (b); thus it descends one level of the helix.

To make our picture more complete, we show how the wave functions evolve along a circuit enclosing B_c (Fig. 4). We define the elliptical contour $B = B_0 \cos\theta$, $\Delta = \Delta_0 \sin\theta$ [Fig. 4(a)], and in Fig. 4(b)-(l) show how a particular resonance—$n = 1$, $m = 5/2$ in Fig. 4(b)—

evolves as a function of θ. For convenience, we use the same adiabatic circuit as in Fig. 2, where θ ranges from π to -π and the state descends the helix by one level, using B_0 = 4 T and Δ_0 = 24 meV. Since the radial motion for fixed m is equivalent to one-dimensional motion in a potential well, let us recall that for the single-component Schrödinger equation, the nth eigenstate is a wave function with n+1 lobes. For these Dirac wells, n can be defined unambiguously only if the lowest positive state is independent of Δ (i.e., for $B < B_c$), and here the "Schrodinger pattern" is followed, in the sense that both components of the Dirac spinor have n+1 radial lobes [Figs. 4(b) and 4(l)]. By contrast, for $B > B_c$ (where $\varphi_B \approx \pi$ and n is ill-defined) the wave functions follow the usual pattern of massless Dirac LLs [36], where the upper component has one more radial lobe than the lower component [Fig. 4(g)] [37]. These LLs can thus be regarded as "half-integer" states, midway between consecutive equal-lobed states with $\varphi_B = 0$.

As we descend the helix, the resonance gradually sheds its outer lobes. In the first half of the circuit [Figs. 4(b)-4(g)], the upper spinor component becomes stronger (as expected for Δ>0), while the lower components's outer lobe fades in intensity and finally disappears, leaving at θ=0 the standard LL-type eigenspinor [Fig. 4(g)]. Returning with negative Δ [Figs. 4(h)-4(l)], the upper component weakens and similarly loses its outer lobe, so that the resulting state [Fig. 4(l)] has one less lobe in each component. For the circuit shown here, the lobe-fading occupies a fairly narrow range of angles [Figs. 4(d),(e);(i),(j)] corresponding to the condition $B \approx B_c$; we find empirically that the more rapid the rate of "lobe shedding" (or adding) along the loop, the shorter the lifetime of the instantaneous resonance [34].

The process depicted in Fig. 4, in which the particle passes adiabatically between what we would normally regard as *different* eigenstates, deserves some discussion in connection with the quantum-mechanical adiabatic theorem [38,39]. For the quadratic confining potential used here, it

was shown [18,34] that throughout the B-Δ plane, the "eigenstates" have the character of resonances with finite lifetimes, to which the theorem does not strictly apply. At high $|B|$, however, the potential could be turned off, and the states would revert to the well-known LLs of the symmetric gauge [36,37]. Then, by turning on the confining potential temporarily together with Δ, we could pass adiabatically to the next higher or lower LL by encircling B_c. This would still not break the adiabatic theorem, since at B_c the confining potential introduces a lifetime of the order e^{Δ^2}: the circuit necessarily passes through a region in which the theorem is inapplicable. The adiabatic timescale could be much shorter than the lifetime, however [27,40,41], and in an experiment (if feasible), all but an exponentially small fraction of particles might traverse the circuit successfully.

In conclusion, we have shown that the resonance manifold of the 2D Dirac equation in a magnetic field and a smooth central potential, instead of consisting of a series of absolutely separated orthonormal states, is topologically defective: It is subtly linked together so that by turning on a mass term and cycling the sign of the field, a particle in one state can be adiabatically promoted level by level up a helical ladder, or downward until it reaches at the bottom a state adiabatically connected to the N=0 LL. A direct experimental exploration of this helix requires a method to independently vary Δ and B, which is experimentally challenging. Possible methods to access Δ in graphene include strain engineering [42], or utilizing moiré superlattice potentials [43,44]. More exotic experimental environments might be sought in cold-atom systems [45,46] or collections of mechanical oscillators [47]. Although a direct experimental exploration of this helix structure may be difficult, the discontinuity at Δ=0 has already been observed in graphene [4], and the physics revealed here is broadly applicable to electron confinement in other 2D Dirac materials.

Acknowledgements:

D.W. acknowledges support under the Cooperative Research Agreement between the University of Maryland and the National Institute of Standards and Technology Center for Nanoscale Science and Technology, Grant No. 70NANB10H193, through the University of Maryland. We thank Michael Zwolak, Mark Stiles, and Joaquin Rodriguez-Nieva for valuable discussions.

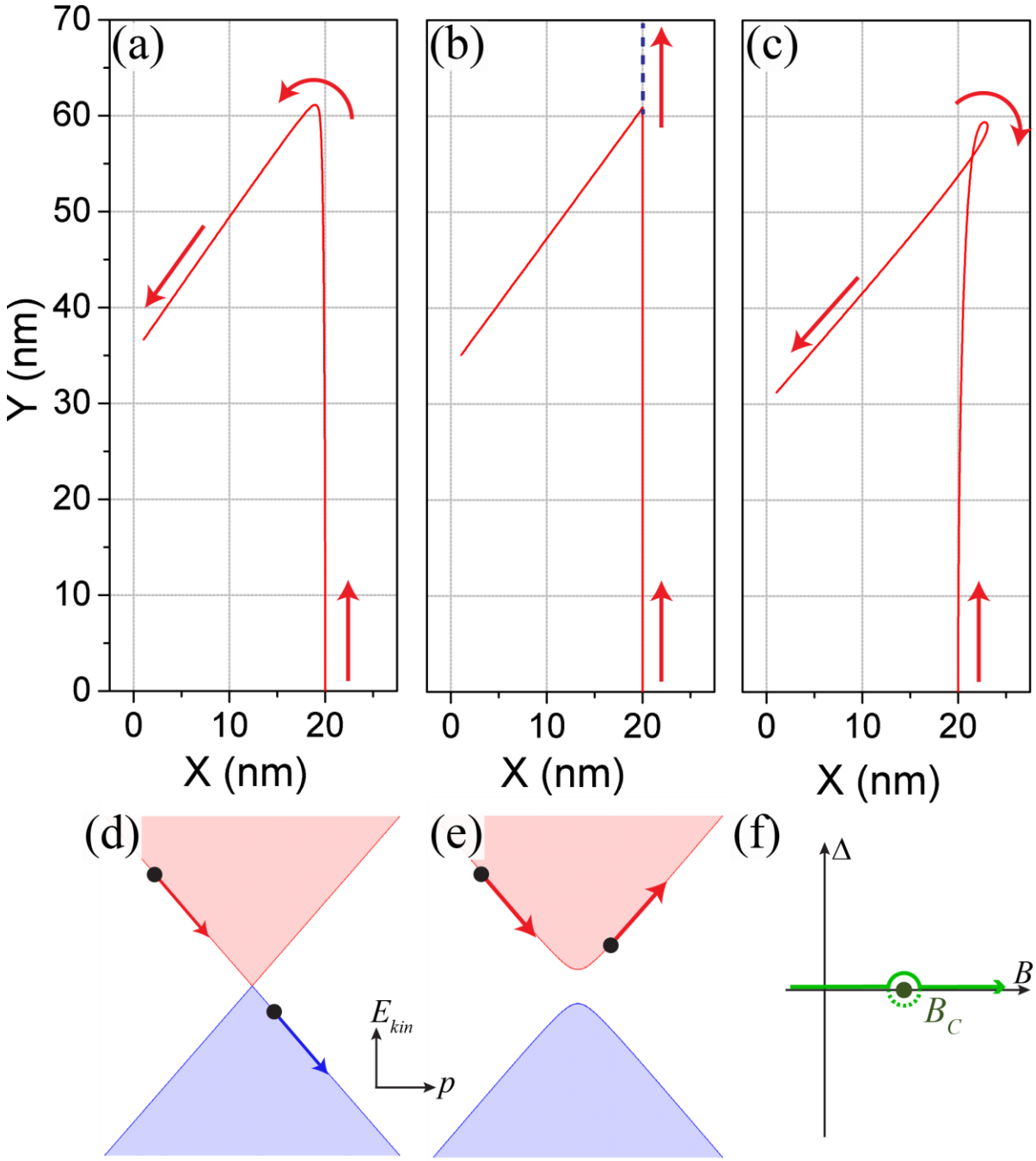

Figure 1: **Classical trajectories near B_c. (a)-(c)** Calculated trajectory of a massless, upward-moving particle released at X=200 Å in magnetic fields slightly less than **(a)**; equal to **(b)**, and greater than **(c)** the critical magnetic field. In (b) the particle escapes by Klein tunneling. **(d)** and **(e)** show the role of the mass in keeping the motion periodic at $B = B_c$: massless particles Klein-tunnel out of the potential well (d), while massive particles remain inside and continue to orbit (e). If the Hamiltonian is varied adiabatically, the path **(f)** must avoid B_c.

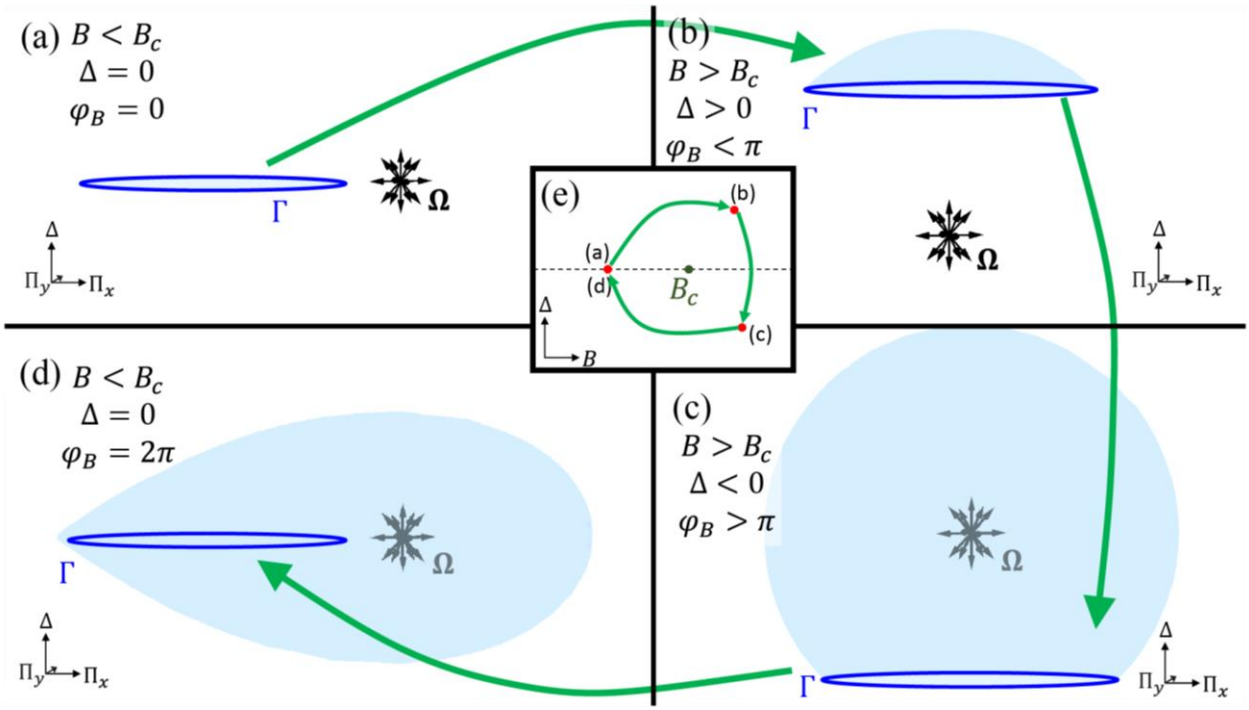

Figure 2:**Adiabatic circuit of the Hamiltonian about B_c.** Panels **(a)-(d)** schematically show the momentum-space contour Γ (thin blue ring), the monopole source of Berry curvature $\boldsymbol{\Omega}$ at the origin, and the solid angle subtended by Γ (light blue sheet). During an adiabatic circuit the ring is pulled over the monopole, and the Berry phase increases by 2π. **(e)**, center, shows the circuit in the B-Δ plane, with the locations of panels **(a)-(d)** indicated by red dots. The direction of the adiabatic loop is indicated by green arrows.

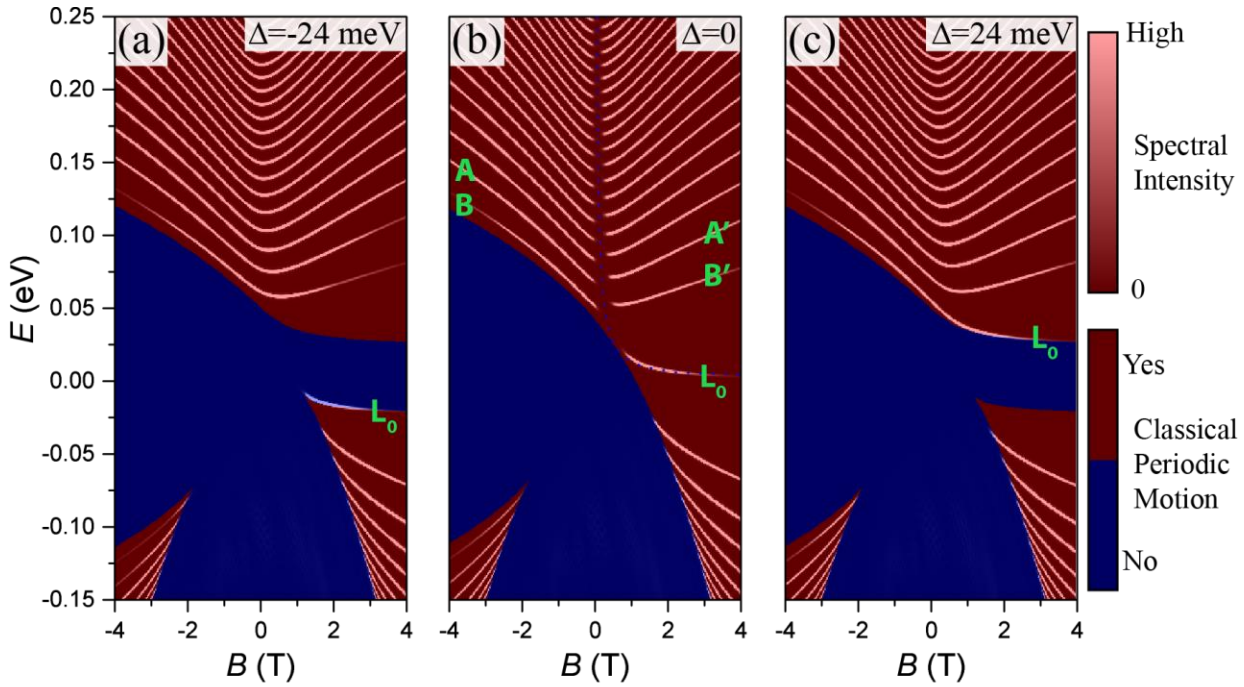

Figure 3: **Screw dislocation in the m=5/2 eigenstate manifold.** Panels **(a)-(c)** show the resonance spectrum of an m=5/2 wavepacket (see main text) as a function of magnetic field for Δ=-24 meV, 0, and +24 meV respectively. Superimposed on the spectrum (dark-bright color scale) are the regions of phase space where classical periodic motion is possible (red) or impossible (blue) as determined by analysis of the classical Hamiltonian [34].

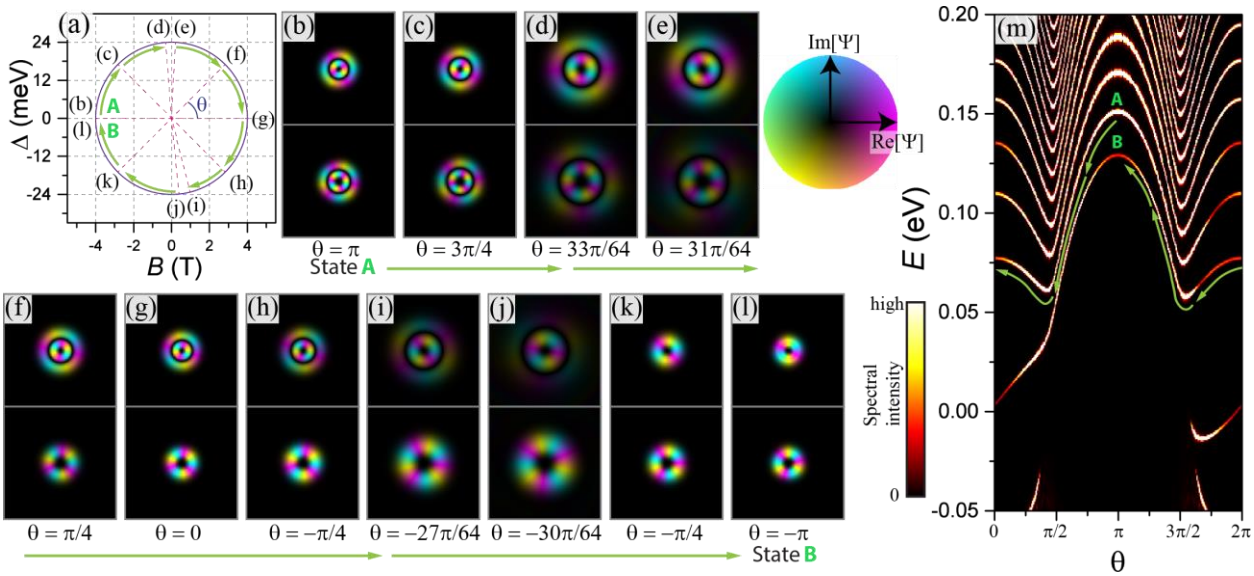

Figure 4: **Evolution of a resonance along an adiabatic loop. (a)** In the B-Δ plane we define the elliptical contour $B = B_0 \cos\theta, \Delta = \Delta_0 \sin\theta$, where B_0=4 T and Δ_0=24 meV (for other parameters of the Hamiltonian see the main text). An adiabatic circuit, identical to that schematized in Fig. 2e, begins at state **A (b)** and proceeds clockwise, arriving at state **B (l)**. The calculated wave functions at intermediate angles are shown in **(c)-(k)**. At positive mass and increasing field (c)-(f), the lower component loses its outer lobe; at negative mass in decreasing field (h)-(k), the upper component loses its outer lobe. In (b)-(l) the subpanel side length is 330 nm; the upper and lower spinor components are shown in the corresponding subpanels. The resonance spectrum as a function of θ is shown in **(m)**, with the path from A to B traced by green arrows.

References:

[1] A. V. Shytov, M. S. Rudner, and L. S. Levitov, Phys. Rev. Lett. **101**, 156804 (2008).

[2] Y. Zhao, J. Wyrick, F. D. Natterer, J. F. Rodriguez-Nieva, C. Lewandowski, K. Watanabe, T. Taniguchi, L. S. Levitov, N. B. Zhitenev, and J. A. Stroscio, Science **348**, 672 (2015).

[3] N. M. Freitag, L. A. Chizhova, P. Nemes-Incze, C. R. Woods, R. V. Gorbachev, Y. Cao, A. K. Geim, K. S. Novoselov, J. Burgdörfer, F. Libisch, and M. Morgenstern, Nano Lett. **16**, 5798 (2016).

[4] F. Ghahari, D. Walkup, C. Gutiérrez, J. F. Rodriguez-Nieva, Y. Zhao, J. Wyrick, F. D. Natterer, W. G. Cullen, K. Watanabe, T. Taniguchi, L. S. Levitov, N. B. Zhitenev, and J. A. Stroscio, Science **356**, 845 (2017).

[5] K. S. Novoselov, A. K. Geim, S. V. Morozov, D. Jiang, M. I. Katsnelson, I. V. Grigorieva, S. V. Dubonos, and A. A. Firsov, Nature **438**, 197 (2005).

[6] Y. Zhang, Y.-W. Tan, H. L. Stormer, and P. Kim, Nature **438**, 201 (2005).

[7] T. Ando, T. Nakanishi, and R. Saito, J. Phys. Soc. Jpn. **67**, 2857 (1998).

[8] A. F. Young and P. Kim, Nat. Phys. **5**, 222 (2009).

[9] J. F. Rodriguez-Nieva and L. S. Levitov, Phys. Rev. B **94**, 235406 (2016).

[10] M. Ezawa, Phys. Rev. B **76**, (2007).
[11] H. P. Heiskanen, M. Manninen, and J. Akola, New J. Phys. **10**, 103015 (2008).
[12] M. Zarenia, A. Chaves, G. A. Farias, and F. M. Peeters, Phys. Rev. B **84**, (2011).
[13] A. Matulis and F. M. Peeters, Phys. Rev. B **77**, (2008).
[14] J. H. Bardarson, M. Titov, and P. W. Brouwer, Phys. Rev. Lett. **102**, 226803 (2009).
[15] A. Matulis, M. Ramezani Masir, and F. M. Peeters, Phys. Rev. A **86**, (2012).
[16] M. Ramezani Masir, A. Matulis, and F. M. Peeters, Phys. Rev. B **84**, (2011).
[17] H.-Y. Chen, V. Apalkov, and T. Chakraborty, Phys. Rev. Lett. **98**, 186803 (2007).
[18] G. Giavaras, P. A. Maksym, and M. Roy, J. Phys. Condens. Matter **21**, 102201 (2009).
[19] J. Lee, D. Wong, J. Velasco Jr, J. F. Rodriguez-Nieva, S. Kahn, H.-Z. Tsai, T. Taniguchi, K. Watanabe, A. Zettl, F. Wang, L. S. Levitov, and M. F. Crommie, Nat. Phys. **12**, 1032 (2016).
[20] M. I. Katsnelson, K. S. Novoselov, and A. K. Geim, Nat Phys **2**, 620 (2006).
[21] V. V. Cheianov, V. Fal'ko, and B. L. Altshuler, Science **315**, 1252 (2007).
[22] P. E. Allain and J. N. Fuchs, Eur. Phys. J. B **83**, 301 (2011).
[23] F. Sauter, Z. Für Phys. **73**, 547 (1932).
[24] L. Landau,L.D. E. M., *Mechanics*, 3rd ed. (Butterworth-Heinemann, 1982).
[25] D. Xiao, M.-C. Chang, and Q. Niu, Rev. Mod. Phys. **82**, 1959 (2010).
[26] G. P. Mikitik and Y. V. Sharlai, Phys. Rev. Lett. **82**, 2147 (1999).
[27] M. V. Berry, Proc. R. Soc. Lond. Math. Phys. Eng. Sci. **392**, 45 (1984).
[28] A. Einstein, Deutshe Phys. Ges. **19**, 82 (1917).
[29] A. D. Stone, Phys. Today **58**, 37 (2005).
[30] M. D. Feit, J. A. Fleck, and A. Steiger, J. Comput. Phys. **47**, 412 (1982).
[31] A. D. Bandrauk and H. Shen, Chem. Phys. Lett. **176**, 428 (1991).
[32] J. A. Fleck, J. R. Morris, and M. D. Feit, Appl. Phys. **10**, 129 (1976).
[33] A. Chaves, G. A. Farias, F. M. Peeters, and R. Ferreira, Commun. Comput. Phys. **17**, 850 (2015).
[34] See Supplemental Material at [URL] for details of numerical methods and semicalssical analysis.
[35] F. D. M. Haldane, Phys. Rev. Lett. **61**, 2015 (1988).
[36] M. O. Goerbig, Rev. Mod. Phys. **83**, 1193 (2011).
[37] Y.-S. Fu, M. Kawamura, K. Igarashi, H. Takagi, T. Hanaguri, and T. Sasagawa, Nat. Phys. **10**, 815 (2014).
[38] T. Kato, J. Phys. Soc. Jpn. **5**, 435 (1950).
[39] M. Born and V. Fock, Z. Für Phys. **51**, 165 (1928).
[40] M. V. Berry, J. Phys. Math. Gen. **17**, 1225 (1984).
[41] J. Hwang and P. Pechukas, J. Chem. Phys. **67**, 4640 (1977).
[42] F. Guinea, M. I. Katsnelson, and A. K. Geim, Nat Phys **6**, 30 (2010).
[43] D. L. Miller, K. D. Kubista, G. M. Rutter, M. Ruan, W. A. de Heer, M. Kindermann, P. N. First, and J. A. Stroscio, Nat. Phys **6**, 811 (2010).
[44] M. Kindermann, B. Uchoa, and D. L. Miller, Phys. Rev. B **86**, 115415 (2012).
[45] L. Tarruell, D. Greif, T. Uehlinger, G. Jotzu, and T. Esslinger, Nature **483**, 302 (2012).
[46] S. Nakajima, T. Tomita, S. Taie, T. Ichinose, H. Ozawa, L. Wang, M. Troyer, and Y. Takahashi, Nat. Phys. **12**, 296 (2016).
[47] S. D. Huber, Nat. Phys. **12**, 621 (2016).

Supplementary information for

Helical Level Structure of Dirac Potential Wells

Daniel Walkup[1,2†] and Joseph A. Stroscio[1]

[1]Center for Nanoscale Science and Technology, National Institute of Standards and Technology, Gaithersburg, MD 20899, USA
[2]Maryland NanoCenter, University of Maryland, College Park, MD 20742, USA

Contents

† To whom correspondence should be addressed.

1. Quadratic potential - possibility of classical periodic motion

For the quadratic potential well, we can explicate the classical phase diagram of the electron motion using the mathematics of cubic functions. This allows us to generate the colored backgrounds of Fig. 3, and gain some other insights as well. The square of the radial momentum,

$$p_r^2(r) = \left(\frac{E - \kappa r^2}{v_F}\right)^2 - \left(\frac{p_\phi}{r} - \frac{eB}{2}r\right)^2 - \Delta^2, \qquad (S1)$$

can be expressed in terms of $s \equiv r^2$ as

$$f(s) \equiv s p_r^2(s) = as^3 + bs^2 + cs + d \qquad (S2)$$

where $a = (\kappa/v_F)^2$, $b = -(2E\kappa/v_f^2 + e^2B^2/4)$, $c = (E/v_F)^2 - \Delta^2 + ep_\phi B$, and $d = -p_\phi^2$. We have $f(0) = -p_\phi^2$, $f(s \to \infty) = +\infty$, so that f has at least one real root for positive s. The number of real roots is determined by the discriminant, $D = 18abcd - 4b^3d + b^2c^2 - 4ac^3 - 27a^2d^2$. A sign change of the discriminant signifies the transition from the one-root regime ($D < 0$) to the three-root regime ($D > 0$) with a double root occurring for $D = 0$ (**Fig. S1**). Physically, classical periodic motion occurs in the three-root regime between the first two roots [1] (**Fig. S1(a, d)**).

In the three-root regime the area between the first two roots relates to the classical action $J_r = \oint p_r dr$, and the area between the second two is related to the WKB tunneling integral $P = \int |p_r(r)| dr$; these labels are included in **Fig. S1**. A sign change of D can occur in two physically distinct ways, depending on which pair of roots merge together and vanish. When the first pair merges (**Fig. S1(a-c)**), the action goes to zero: we reach the bottom of a ladder of eigenstates. The merging of the second pair (**Fig. S1(d-f)**) signifies the lifetime going to zero: the particle escapes and the resonances line disappears. In **Figs. S1,2** we label the first type of transition **I**, and the second type **II**.

In **Fig. S2** we show planar "phase diagrams" of the Hamiltonian for $m = 5/2$, κ= 4 eV/μm^2, and $\Delta = 0, \pm 24$ meV. The three-root regime is shown in red and the one-root regime in blue; zeroes of D, which is calculated numerically, are shown as bright curves. At finite mass **Fig. S2(b)**, all such zero-curves correspond to transitions between the one-root and three-root regimes, except one a pair of curves labeled **IV**, which correspond to roots appearing unphysically at negative s. The three-root regime is split into regions labeled (1), (2) and (3). Region (1) is the region of quasi-bound orbits of the type discussed in the main text (**Fig. 1**), and regions (2) and (3) contain states corresponding to negative Landau levels. At positive field, the gap between regions (1) and (3) is about 2|Δ|, and disappears when Δ=0 (**Fig. S1(a)**). At zero mass, region (1) is bisected by the bright curve labeled **II**$'$, which is the cricital field: $B_c(E) = 2\kappa m\hbar/E$. Crossing this curve from left to right, the lifetime goes to zero and then comes back (**Fig. S1(d,e)**), the Berry phase having switched from 0 to π. We note here that in **Fig. S2(b)** the equation $B_c(E) = 2\kappa m\hbar/E$ describes both **II**$'$ and its extension, labeled **I**$'$, which is a zero-locus of the radial action; on this locus sits the state L_0, which corresponds to the N=0 Landau level (**Fig. S2(d)**).

To link this discussion up with the main text, in **Fig. S2(c-e)** we superimpose the calculated resonance spectra on the phase diagram. Of course, resonances only occur in the three-root regime. As explained in the main text, the helix structure emerges from the fact that for $\Delta < 0$, L_0 sits on the top of region (3) (**Fig. S2(c)**), whereas for $\Delta > 0$ it is at the bottom of region (1) (**Fig. S2(e)**).

2. Generating the initial wavepacket

The spectra shown in Fig. 3 were extracted using a picked wavepacket, described below. But the energy levels obtained from the spectral method are quite independent of the initial wavefunction. To show this, we first describe some methods for generating randomized wavepackets (**Fig. S3**), and show the spectral results obtained using such wavepackets (**Fig. S4**).

In constructing an initial wavepacket χ_0 with a given m it is important to adhere to certain requirements. For the radially symmetric spinor

$$\chi_m(\mathbf{r}) = e^{i\left(m-\frac{1}{2}\right)\phi}\begin{pmatrix} u_0(r) \\ e^{i\phi}u_1(r) \end{pmatrix} = \begin{pmatrix} e^{i\left(m-\frac{1}{2}\right)\phi}u_0(r) \\ e^{i\left(m+\frac{1}{2}\right)\phi}u_1(r) \end{pmatrix}, \qquad (S3)$$

each component will be some $F_n(r,\phi) = e^{in\phi}u(r)$; these are inherently orthogonal for different n. Because the simulation is on a Cartesian pixel grid, the orthogonality is only approximate: the aliasing of $e^{in\phi}$ near $r = 0$ creates overlap between different n unless $u(r)$ is suppressed near the origin.

This necessity of suppressing $F_n(r,\phi)$ near r=0 coincides with the physical suppression of the wave function for orbits with large angular momentum. Naively, we can use well-known sets of orthonormal functions, for example associated Laguerre functions [2]

$$M_n^p(r,\phi) = e^{in\phi}L_{n+p}^n(x)e^{-\frac{x}{2}}, \qquad (S4)$$

where $x = \left(\frac{r}{r_0}\right)^2$, r_0 is a parameter, and $L_{n+p}^n(x)$ is the associated Laguerre polynomial. We can then form F_n as

$$F_n(r,\phi) = \sum_{p=0}^{p_{max}} c_p M_n^p(\mathbf{r}) \qquad (S5)$$

where the c_p are chosen in some random manner, and p_{max} is on the order of the number of linear pixels in the simulation area.

With Laguerre functions it is possible to prevent spatial aliasing, and also to explore a large region of momentum space, by tuning r_0. To do this, we take advantage of the fact that the Fourier transform of the normalized Laguerre function is a re-scaled version of the same function in momentum space: As p increases, the function $L_{n+p}^{n}(x)e^{-x/2}$ expands towards the edge of the simulation grid, and its Fourier transform expands towards the edge of the 2D Brillouin zone. We choose r_0 such that the real and momentum-space Laguerre functions "touch" the edge of their respective spaces at the same value of p, then choose a somewhat smaller p_{max}.

We can also use the Laguerre functions as an orthonormal basis for projecting other wavefunctions, which we initially randomize without regard to their angular momentum. Such wave functions can be formed easily in momentum-space, by filling all **k** up to some k_{max} with random phase factors:

$$\chi_{\mathbf{k}} = \begin{pmatrix} e^{iR_1} \\ e^{iR_2} \end{pmatrix} \qquad (S6)$$

where $R_{1,2}$ are random numbers between zero and 2π. An example of such a wave-function formed in a 128x128 pixel grid is shown in **Fig. S3(b)**. Its inverse Fourier transform—that is, the real space wave function—is shown in **Fig. S3(c)**, and its projection onto the m=5/2 subspace is shown in **Fig. S3(d).** Resonance spectra as a function of field for three randomized wavepackets generated by this method are shown in **Fig. S4(a)-(c)**, together with the average of the three spectra (**Fig. S4(d)**).

The noticeable dips in the resonance intensity in **Fig. S4(a)-(c)** can be explained as matrix element effects: as the Hamiltonan changes the eigenstates change gradually, and because the randomized wavepacket represents only one vector of the Hilbert space, some of these eigenstates

sweep through a state of orthogonality or near-orthogonality to χ_m. These dips are less common for the picked wavefunction.

For the spectra shown in **Fig. 3** and **Fig. 4(m)** we used the picked function

$$\chi_m(\mathbf{r}) = e^{i\left(m-\frac{1}{2}\right)\phi} \begin{pmatrix} G(r)F(r) \\ e^{i\phi+\alpha}G(r)F(r) \end{pmatrix} e^{iwr^2} \qquad (S7)$$

where $G(r) = \frac{1}{2}\left(1 + \mathrm{erf}\left(\frac{(r-r_{\min})}{L_1}\right)\right)$ is a Gaussian error function designed to eliminate aliasing effects by suppressing the wavefunction below radius $r_{\min}$, $F(r) = 1/(1 + e^{(r-r_{\max})/L_2})$ is a Fermi function which cuts off the wavefunction at radius $r_{\max}$, w is a constant so chosen that the local wavenumber $2wr$ approaches the Brillouin zone edge by $r_{\max}$, and the roll-off lengths L_1 and L_2 are on the order of two pixels. The constant α influences the initial velocity distribution: F and G being real functions, α=0 would correspond to an initial velocity radially outward. To obtain good matrix elements with circulatory resonances, we set α=π/2. This wavefunction, generated on a 256x256 pixel grid, is shown in **Fig. S3(a)**.

3. Adiabatic circuits as a function of time

As a secondary part of our simulations we did a two-step calculaton: first, at a given point (B_i, Δ_i), we extract the wave function of a particular resonance, and then we evolve this wave function in a time-dependent Hamiltonian $H(t)$ which starts from that point and slowly moves through the B-Δ plane. This allows us to follow a quantum state as it evolves dynamically along the type of adiabatic loop discussed in the main text.

Fig. S5 and **S6** show results obtained using the elliptical loop defined by $\mathrm{B} = \mathrm{B}_0 \cos\theta$, $\Delta = \Delta_0 \sin\theta$, where B_0=1 T and Δ_0 = 64 meV. (See also supplementary movies 2 and 3). In Fig.

S7 we ascend the eigenstate spiral by putting $\theta = \omega t$; in **Fig. S5** we put $\theta = -\omega t$ to descend the spiral. In both simulations the wavepacket is started in the state analogous to the positive-field N=3 LL (i.e. at $\theta = 0$), and the simulation is run for 40 ps with $\omega = 2\pi/10$ ps. The gradual addition (**Fig. S5**) or subtraction (**Fig. S6**) of outer lobes of the wave function is consistent with the picture of Fig. 4. On the descending path (**Fig. S5**), the state finally delocalizes after slightly more than three circuits. The point of delocalization is, schematically, the "apex" of region (3) of the semiclassical phase diagram (labeled **III** in **Fig. S2(e)**).

We also computed stationary states along this loop as a function of θ, as in Fig. 4. (**Fig. S7**). For the parameters B_0=4 T and Δ_0 = 24 meV used in the main text, the lifetime was noticeably shorter near $\theta=\pi/2$ or $3\pi/2$ than θ=0 or π. In this loop however, the lifetime is more uniform and the growth of the outer lobe proceeds more evenly as a function of θ (**Fig. S7(b)-(q),(r)-(aa)**).

4. Conical and cubic potentials

For completeness, we performed calculations like those of Fig. 3 (with $m = 5/2$) in a conical potential $U = Fr$ where F=800 meV/μm (**Fig. S8(a)-(g)**), the already-shown quadratic potential with κ= 4 eV/ μm^2 (**Fig. S8(h)-(n)**), and a cubic potential $U = Kr^3$ where K = 20 eV/ μm^3 (**Fig. S8(o)-(u)**) as a function of Δ and B. As expected, the same helical resonance spectrum is present in all cases. This is expected theoretically, and in Ref. [3] the zero-mass delocalization at B_c was derived for a generic power-law potential.

5. Zero-Berry phase Landau levels

For $B < B_c$ the Berry phase is zero, and the resonances have equal numbers of radial lobes in their two components (e.g. **Fig. 4(b),(l)**). If we turn off the confining potential, these go into

negative-field LLs with the same property (**Fig. S9(e),(f)**). Because these states are the time-reversal conjugates of negative-m LLs [4,5], we have the seemingly new result that such LLs have zero Berry phase. This can be seen from a semiclassical analysis of the Hamiltonian (following section 1). Taking Eq. (S1) and setting $\kappa = \Delta = 0$ we obtain

$$p_r^2(r) = \left(\frac{E}{v_F}\right)^2 - \left(\frac{m\hbar}{r} - \frac{eB}{2}r\right)^2. \qquad (S8)$$

Again defining $s = r^2$ and $f(s) \equiv s p_r^2(s)$, we have

$$f(s) = as^2 + bs + c \qquad (S9)$$

where $a = -e^2B^2/4$, $b = eBm\hbar + \eta$, $c = -(m\hbar)^2$,and $\eta = E^2/v_f^2$. This f is a downward-curving parabola, and the zero-J_r locus, which is the bottom of the eigenstate ladder, will occur at those energies where the discriminant $D \equiv b^2 - 4ac = 0$. This yields $\eta^2 + 2\eta eBm\hbar = 0$, with solutions $\eta = 0$ and $-\eta = 2eBm\hbar$. The latter root yields real E if $eBm < 0$, in which case

$$E_0 = \pm\sqrt{2v_f^2 e\hbar|m|B}. \qquad (S10)$$

Since m is a half-integer, the allowed Landau levels are at $N = |m| + n + \frac{1}{2}$, which corresponds to the zero-Berry phase rule $J_r = \left(n + \frac{1}{2}\right)h$.

It is interesting to note that the qualitative difference in the classical velocity distribution across B_c is reflected in the quantum-mechanical probability current density. To show this, we calculate $\mathbf{J}(\mathbf{r}) = v_F\psi^\dagger(\mathbf{r})\boldsymbol{\sigma}\psi(\mathbf{r})$ [6] for the states **A**,**B**,**A'**,**B'** (**Fig. S9(g)-(j)**). At negative fields the classical particle (**Fig. S10(b)**) has the same sign of azimuthal velocity at both turning points, and the quantum particle's current density has the same sign on its inner and outer lobes (**Fig. S9**

(i),(j)). At positive B the classical azimuthal velocity is inverted at the outer turning point (**Fig. S10(a)**), while the quantum velocity distribution has an inverted outer lobe (**Fig. S9(g),(h)**). For completeness, in the classical case we include the classical momentum-space contours from which φ_B would be calculated (**Fig. S10(c)**).

References

[1] G. Giavaras, P. A. Maksym, and M. Roy, J. Phys. Condens. Matter **21**, 102201 (2009).
[2] A. Wünsche, J. Comput. Appl. Math. **133**, 665 (2001).
[3] H.-Y. Chen, V. Apalkov, and T. Chakraborty, Phys. Rev. Lett. **98**, 186803 (2007).
[4] Murayama,Hitoshi, (n.d.) (http://hitoshi.berkeley.edu/221a/landau.pdf).
[5] M. O. Goerbig, Rev. Mod. Phys. **83**, 1193 (2011).
[6] P. E. Allain and J. N. Fuchs, Eur. Phys. J. B **83**, 301 (2011).

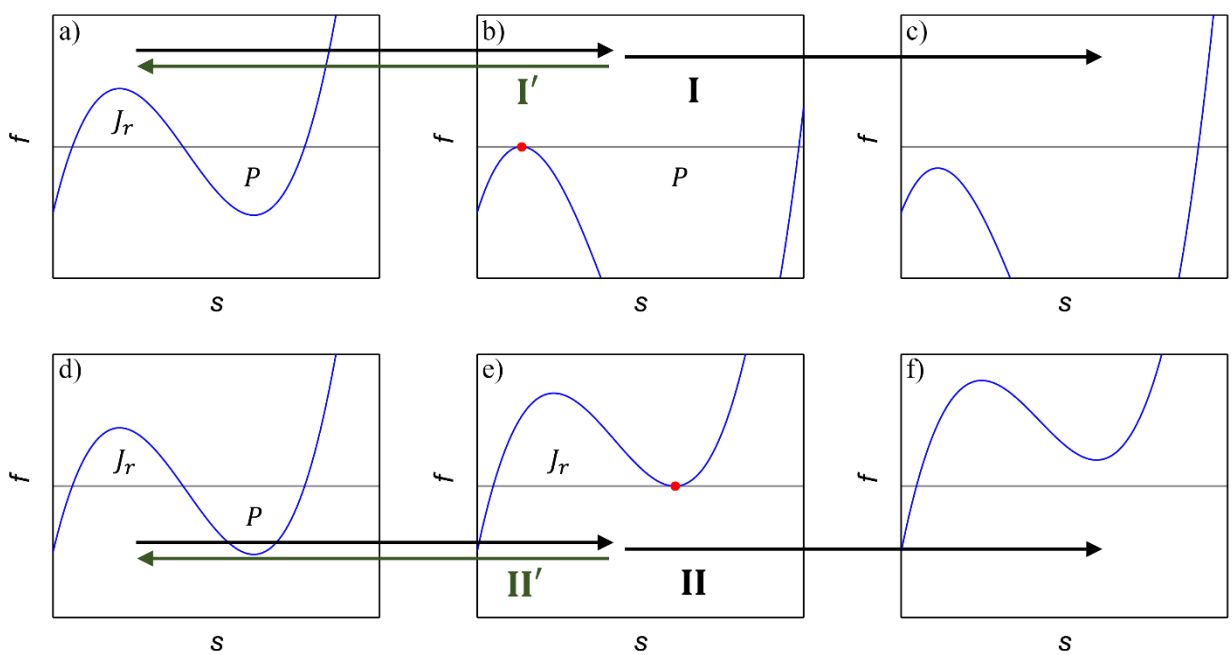

Fig. S1: **Transitions from quasibound to unbound states.** Panels **(a)-(c)** show the dwindling of the radial action, labeled J_r in **(a)**, to zero: the bottom of a ladder of quantum states, the transition is labeled $\boldsymbol{I}$. Panels **(d)-(f)** show the shrinking of the Klein tunneling barrier P to zero, labeled $\boldsymbol{II}$. The "turn-around" behaviors $\boldsymbol{I}'$ and $\boldsymbol{II}'$ are shown in dark green. The curve $f(s)$ is related to the square of the radial momentum: $f(s) = sp_r^2(s)$ where s=r^2.

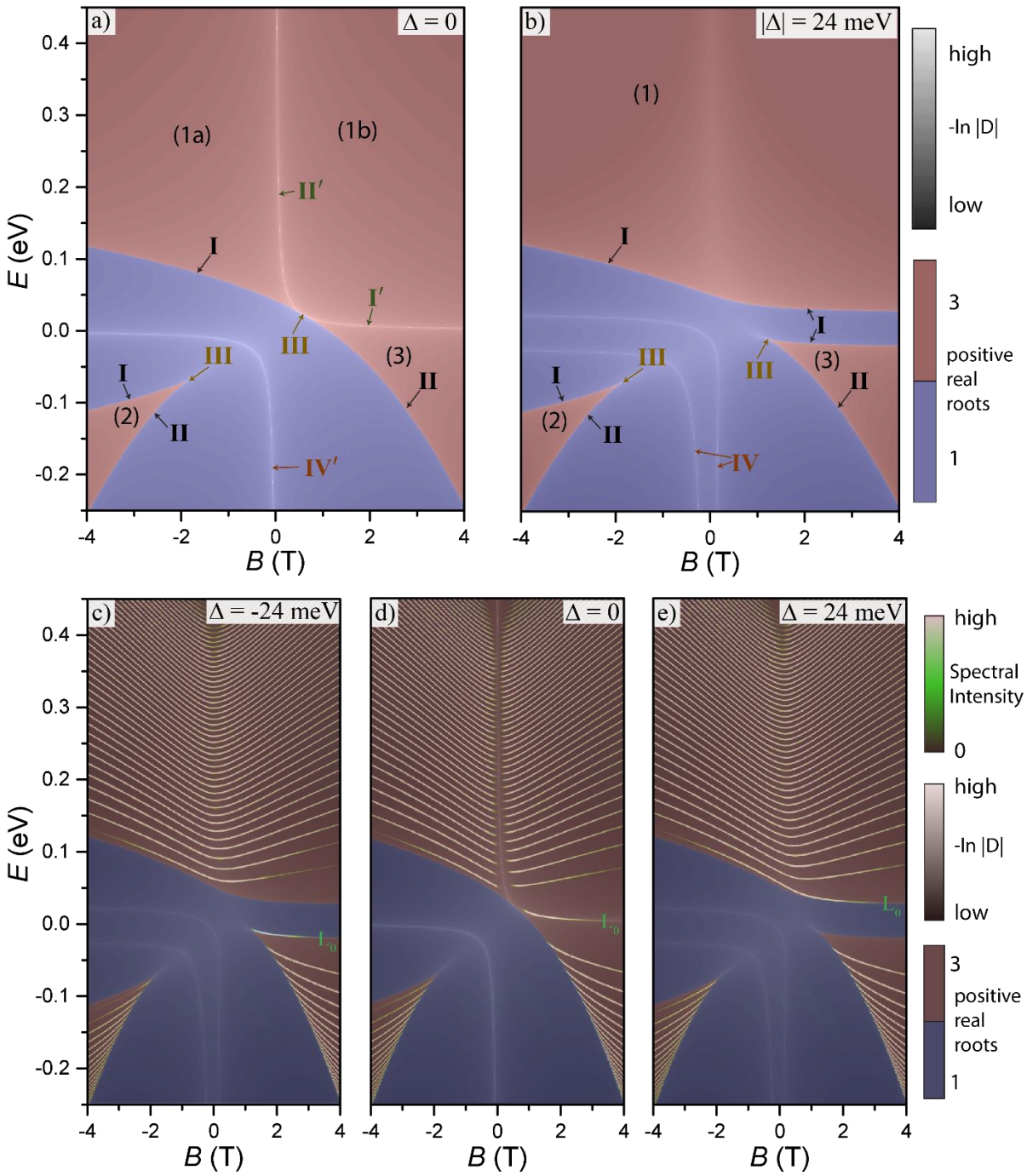

Fig. S2: Semiclassical m=5/2 phase diagram at zero and finite mass. Panels **(a)** and **(b)** show the number of positive roots of $f(s)$ for $m = 5/2$, and the types of transitions between them, (a) for $\Delta = 0$ and (b) $\Delta = 24$ meV, respectively. The foreground is a semitransparent image which is red if $f(s)$ has three positive roots and blue otherwise; divided into regions labeled with Arabic numerals. Zeroes of the discriminant D appear as bright lines. The disconnected red regions for finite Δ (a) are labeled (1),(2),(3); at $\Delta = 0$ (b) region (3) joins region (1), which is split by B_c into regions (1a) and (1b). Classical periodic motion requires 3 real roots. In panels **(c)-(e)** we include also the power spectrum of a picked wavepacket at corresponding masses less than (c), equal to (d), and greater than zero (e); compare Fig. 3 of the main text.

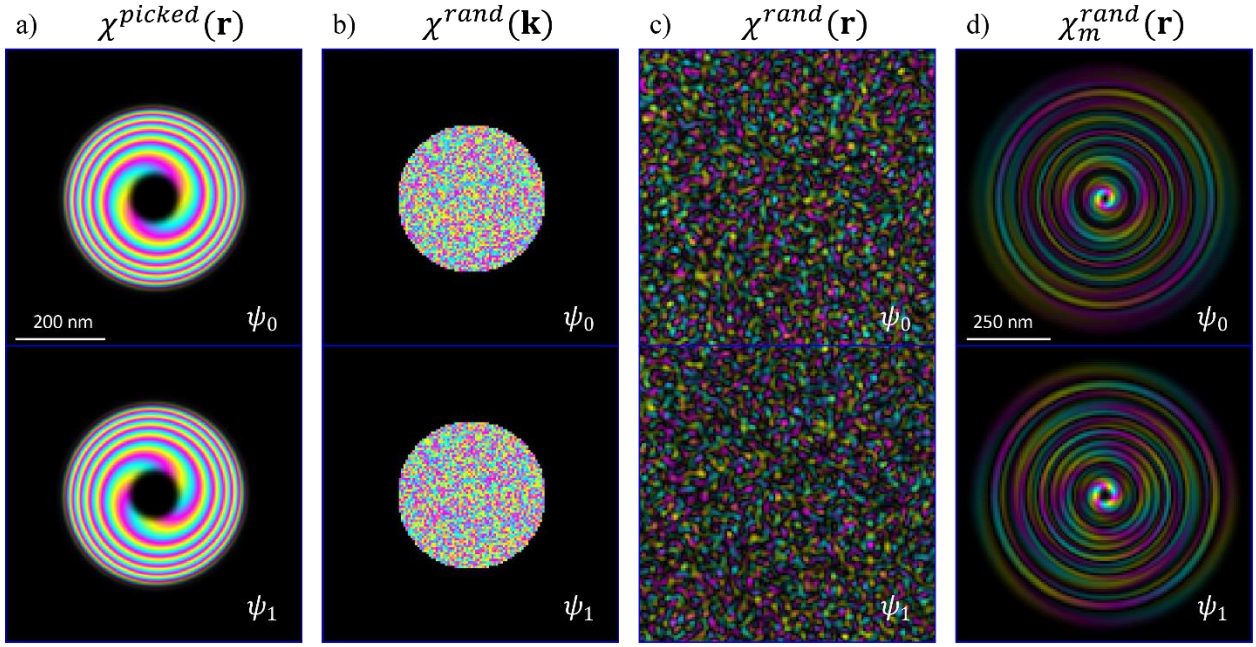

Fig. S3: Initial wavefunctions. (a) shows the "picked" $m = 5/2$ wavefunction used for the dataset of **Figs. 3** and **S2. (b)-(c)** show the steps used in preparing a projected, randomized wavefunction: first the momentum space is filled out with random-phase eigenspinors up to some $k_{\max}$ **(b)**; then we take the inverse Fourier transform **(c)** and project onto the Laguerre subspace for $m = 5/2$ **(d)**. The grids are 256 pixels = 662 nm for **(a)**, 128 pixels = 882 nm for **(c-d)**.

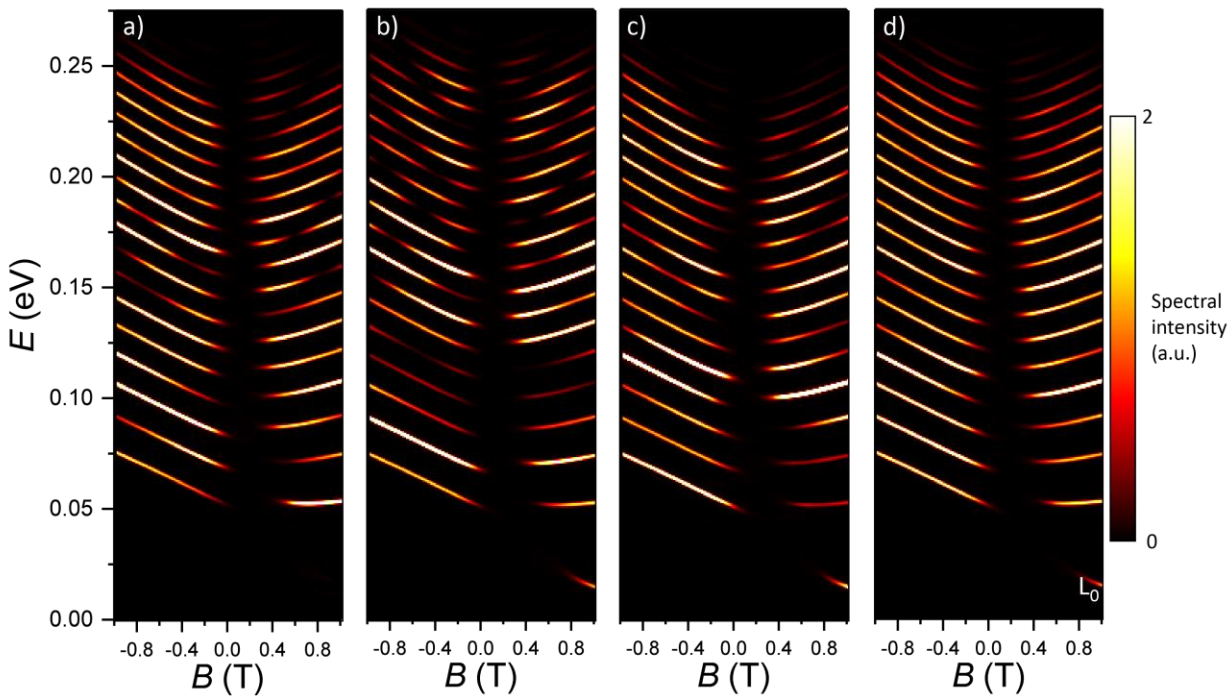

Fig. S4 Power spectra of the correlation function for several initial wavefunctions. Panels **(a)-(c)** show power spectra of $C(t)$ for three different randomized wavefunctions with $m = 5/2$, prepared as described in the text and depicted in **Fig. S3d**. Panel **(d)** shows the average of the three power spectra **(a)-(c)**.

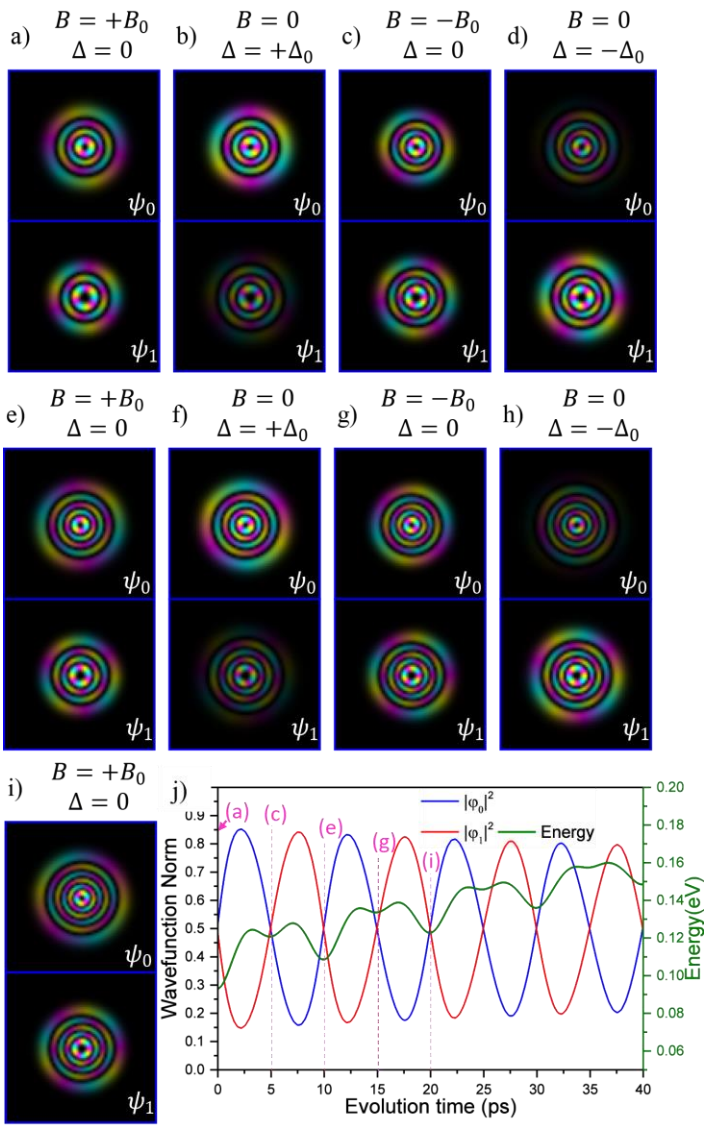

Fig. S5 Adiabatic evolution of a wavepacket ascending the spiral Panels **(a),(b),(c)…(i)** show the two components of the wavefunction after it has evolved through 0,¼,1/2…2 counterclockwise circuits in (B,Δ) space respectively; the time spacing is 2.5 ps. $B_0 = 1$ T, $\Delta_0 = 64$ meV, and each subpanel of **(a)-(i)** has a side length of 440 nm. In the color scale brightness represents amplitude and hue represents phase. **(j)** shows the energy and norm of the wavepacket as it evolves; for every second panel in **(a)-(i)** the snapshot time is indicated by the pink dotted line. The energy, which increases nonmonotonically, is also plotted (green curve).

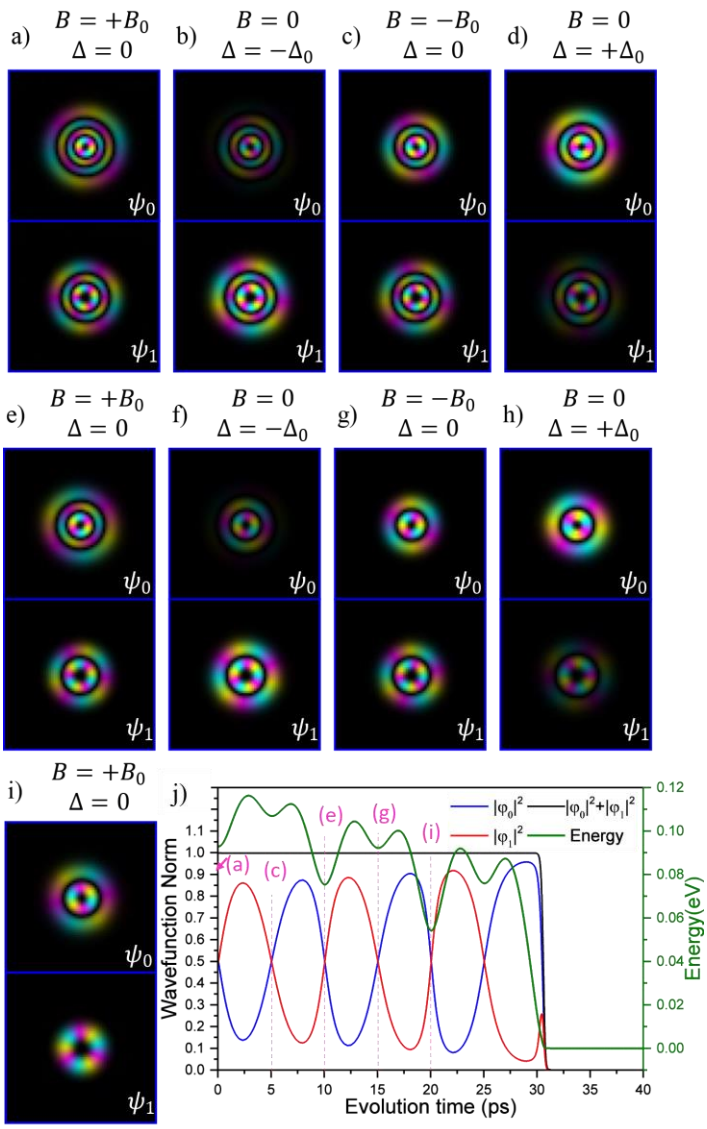

Fig. S6 Adiabatic evolution of a wavepacket descending the spiral. Panels **(a),(b),(c)…(i)** show the two components of the wavefunction after it has evolved through 0,¼,1/2…2 clockwise circuits in (B,Δ) space respectively; the time spacing is 2.5 ps. $B_0 = 1$ T, $\Delta_0 = 64$ meV, and each subpanel of **(a)-(i)** has a side length of 440 nm. In the color scale brightness represents amplitude and hue represents phase. **(j)** shows the energy and norm of the wavepacket as it evolves; for every second panel in **(a)-(i)** the snapshot time is indicated by the pink dotted line. The energy, which increases nonmonotonically, is also plotted (green curve).

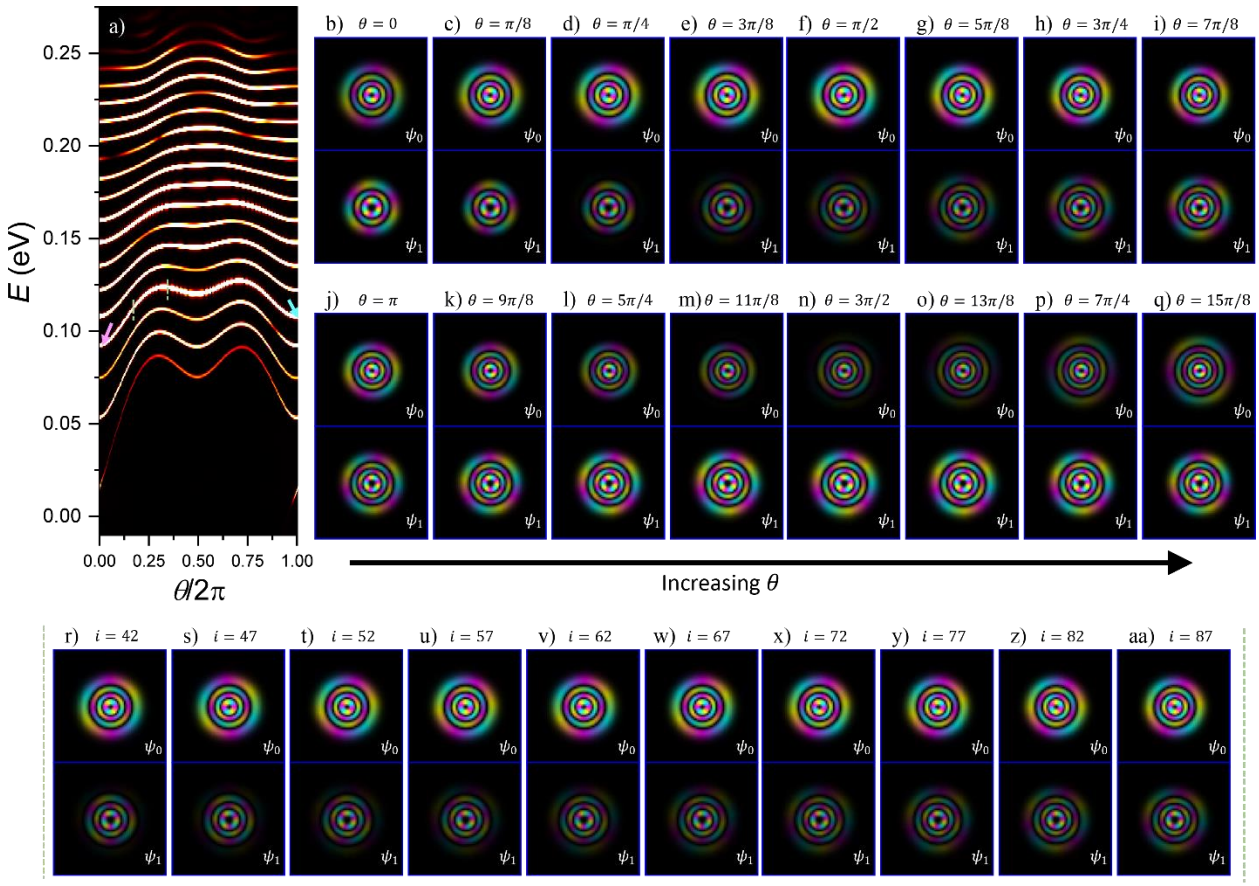

Fig. S7 Weak-field resonances of $\boldsymbol{H(\theta)}$ (a) shows the *m*=5/2 power spectrum of a randomized wavepacket; for $H(\theta)$ we have $B(\theta) = B_0 \cos\theta$, $\Delta(\theta) = \Delta_0 \sin\theta$, $\mathrm{B}_0 = 1$ T, $\Delta_0 = 64$ meV. The pink and cyan arrows point to the same eigenstates as the pink and cyan arrows in **Fig. 3**. To ascend the spiral one may follow the spectrum peak to the right and then zip left along the blue dashed line, and vice versa. Panels **(b)-(q)** show the eigenstates between these arrows at sixteen evenly spaced angles, extracted by Fourier filtration. Panels **(r)-(aa)** show ten eigenstates in a smaller range of angles near $\pi/2$, indicated by the green dashed lines in **(a)**; the lobe gradually builds on the lower component. The index i indicates θ, using $\theta = 2\pi i/256$. The color scale is the same for panels **(b)-(aa);** brightness represents amplitude and hue represents phase.

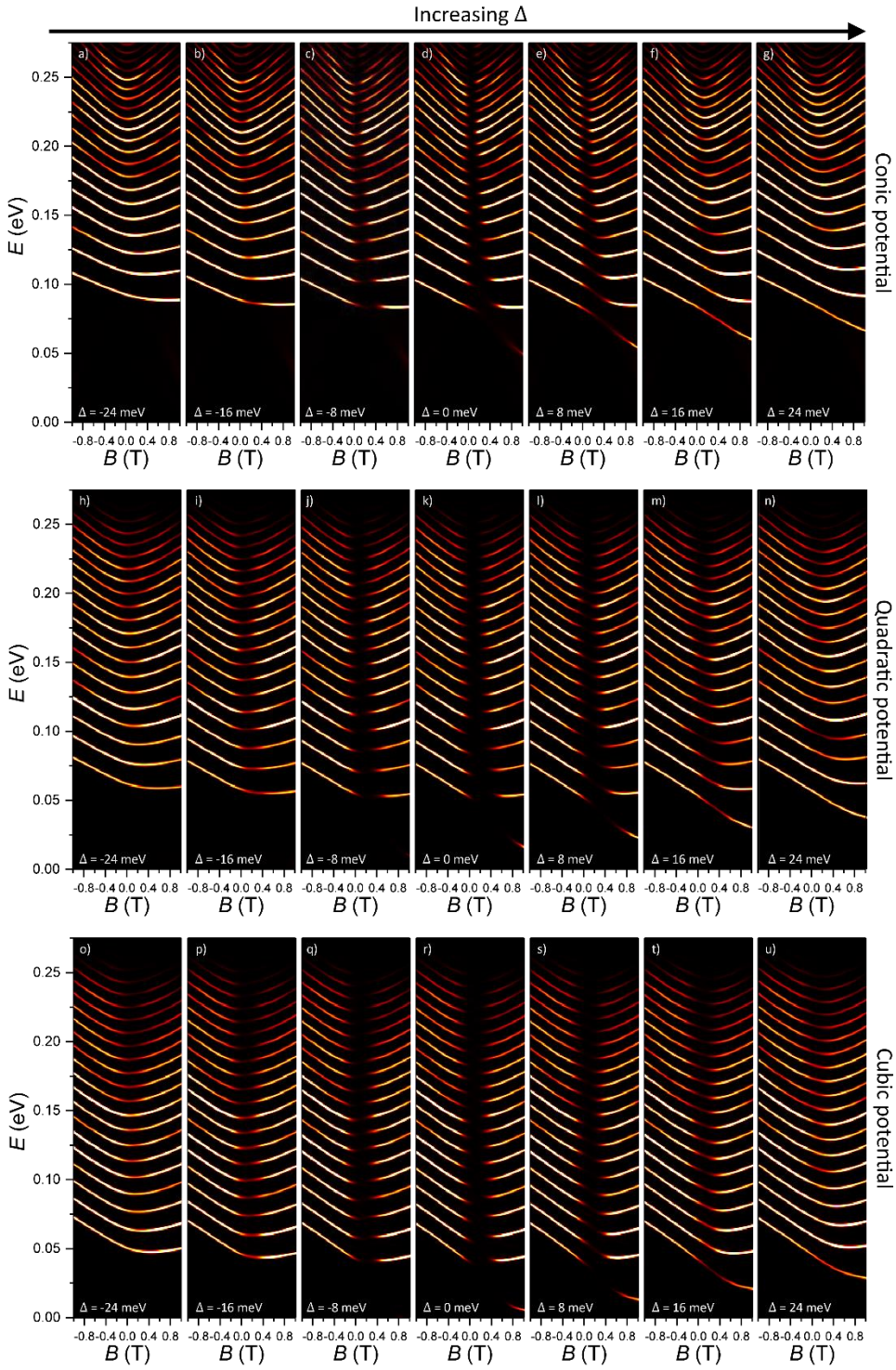

Fig. S8 Helical spectra of power-law potentials. Each panel shows power spectra averaged over a few randomized m=5/2 initial wavefunctions for the indicated mass and well type. Panels **(a)-(g)** use conic potential $U = Fr$ where F=800 meV/μm; panels **(h)-(n)** use a quadratic potential with κ = 4 eV/ μm^2 (the same as elsewhere in the text); panels **(o)-(u)** use a cubic potential $U = Kr^3$ where K = 20 eV/ μm^3.

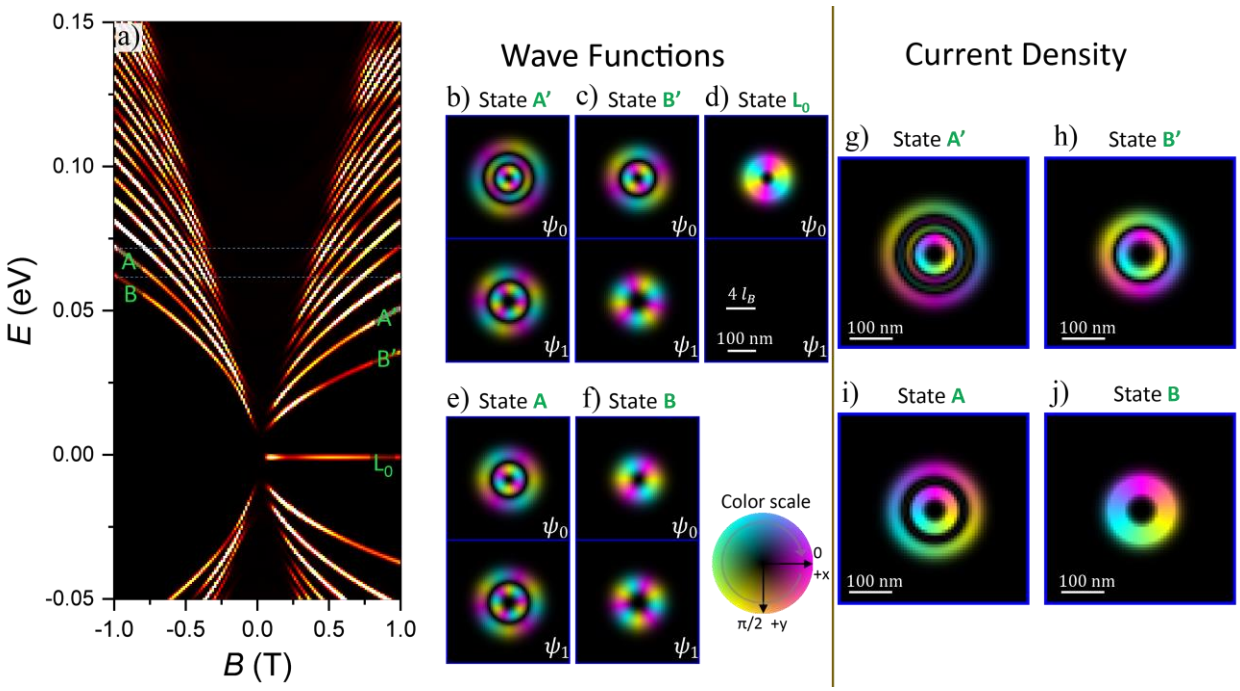

Fig. S9 *m*=5/2 Landau levels at positive and negative magnetic field. Panel **(a)** shows a spectrum as a function of magnetic field for *m*=5/2; the mass and confining potential are zero. The Fourier-extracted wavefunctions corresponding to the states **A**,**B**, **A'**,**B'**,**L₀** at $|B|$ = 1 T are shown in panels **(b)-(f)** respectively. The current density profile $\mathbf{J} = v_F \psi^\dagger \boldsymbol{\sigma} \psi$ is shown in panels **(g)-(j)** for the corresponding states. The wavefunctions are extracted at 1 T, where $l_B = \sqrt{\hbar/eB}$ = 25.7 nm.

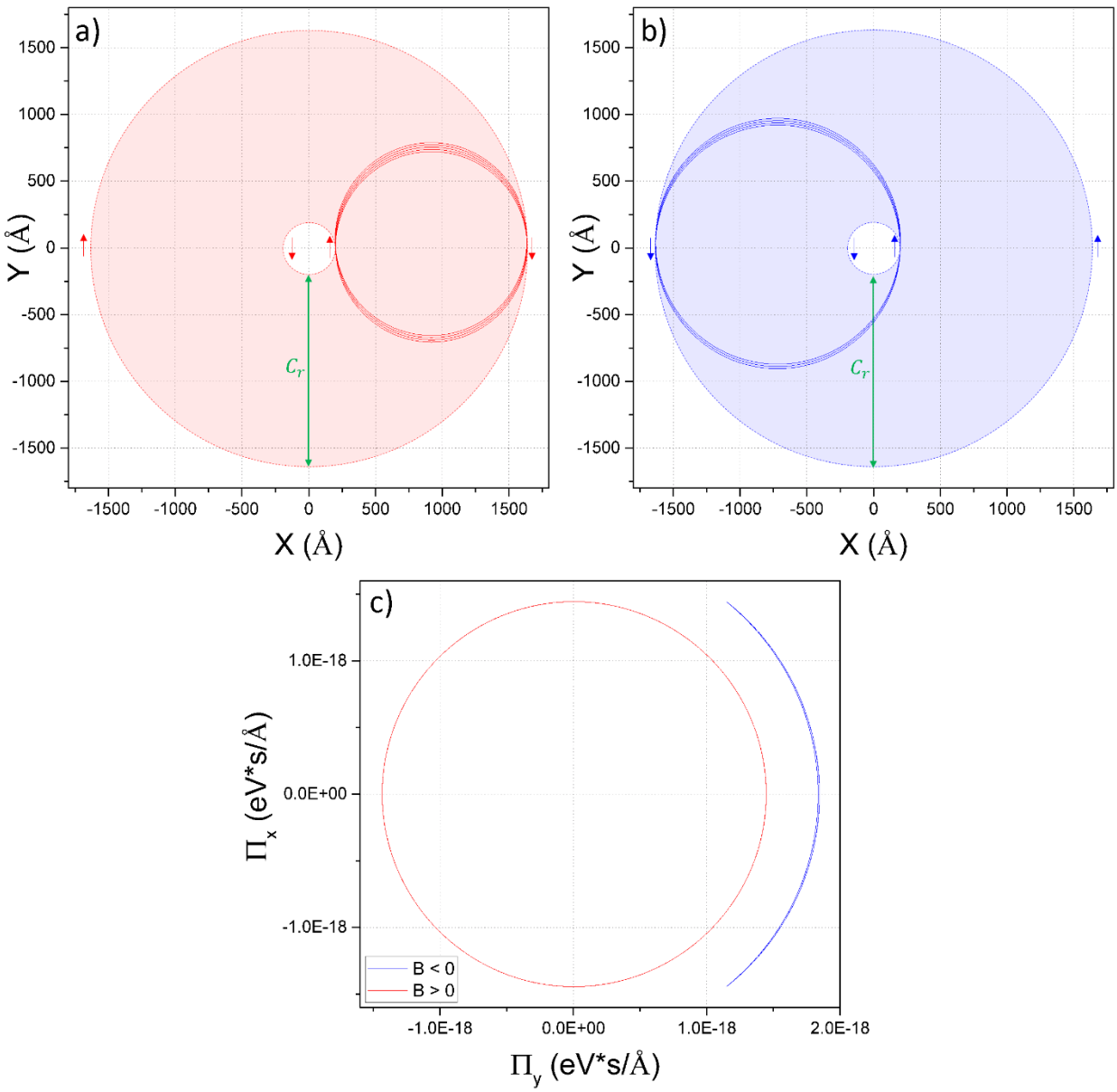

Fig. S10 Classical Landau orbits at positive and negative field. Panels **(a)** and **(b)** show the trajectories of a Dirac particle with angular momentum $+\hbar/2$ released at x=200Å in the potential $U = \kappa r^2$ where κ= 4meV/ μm^2, and B = +200 mT and -200 mT respectively. **(c)** shows the kinematic momentum evaluated along C_r for both orbits. The red orbit picks up a Berry phase of π; the blue crescent-shaped loop does not enclose the origin. The direction of the velocity at the inner and outer turning points is indicated by arrows in **(a)** and **(b)**.

Movie: Helical spectrum of a quadratic potential well (m=5/2). A 3D slice-rendering of the resonance spectrum of the 2D Dirac Hamiltonian in a quadratic potential well (κ=4 eV/μm^2) in the volume defined by B, Δ, and energy E; resonances appear as bright curves. The orthogonal planes are: (1) the Δ-E plane, upper left; (2) the B-E plane, initially lower left, and (3) the B-Δ plane, initially at bottom. First, the B-E plane moves from Δ=+32 meV to -32 meV, following the evolution of Fig. 3(a)-(c) but in reverse order. Then the B-Δ plane increases in energy, showing the eigenstates/resonances as part of a continuous spiral, emanating from the screw dislocation at the critical field B_c. Resonances were obtained using the spectral method (Ref. 30) as described in the main text, using a randomized initial wave packet with m=5/2.